Earth and Planetary Science Letters 303 (2011) 291–298

Contents lists available at ScienceDirect

Earth and Planetary Science Letters

journal homepage: www.elsevier.com/locate/epsl

Large contrasts in crustal structure and composition between the Ordos plateau and the NE Tibetan plateau from receiver function analysis

Suzhen Pan [a,b,*], Fenglin Niu [b]

[a] Geophysical Exploration Center, China Earthquake Administration, 75 Wenhua Road, Zhengzhou, Henan 450002, China
[b] Department of Earth Science, Rice University, 6100 Main Street, Houston, TX 77005, USA

ARTICLE INFO

Article history:
Received 6 October 2010
Received in revised form 6 January 2011
Accepted 8 January 2011
Available online 5 February 2011

Editor: P. Shearer

Keywords:
Tibetan plateau
Ordos plateau
low crustal flow
receiver function
Vp/*Vs* ratio

ABSTRACT

We analyzed thousands of receiver-function data recorded by 154 national and regional seismic stations to study the crustal structure beneath the Ordos plateau and the NE margin of the Tibetan plateau. Moho depth and average crustal *Vp*/*Vs* ratio were measured at each station. The Ordos plateau and the Trans-North China Orogen east of the Ordos are underlain by a moderately thick crust of ~42 km. The Weihe Graben lying at the southern edge of the Ordos plateau has a thin crust of ~30 km, while its southern neighbor, the Qinling orogenic belt shows a thick crust extending to as much as 45 km deep. The Moho depth beneath the NE margin of the Tibetan plateau varies from 55 to 65 km. We found a remarkable contrast between the Tibetan and Ordos plateaus in the measured Poisson's ratio: the Ordos plateau is featured by a high Poisson's ratio while the Tibetan margin has a very low Poisson's ratio. In general, mafic lower crustal rocks have a higher Poisson's ratio than felsic ones. The measured low Poisson's ratio beneath the NE margin of the Tibetan plateau thus indicates that the crustal column beneath the margin is rather felsic, which seems to be inconsistent with a scenario of an inflated crust due to extrusion of lower crust material from the Tibetan plateau to the margin.

1. Introduction

The Ordos plateau located in northern China is an uplifted basin known as the Ordos basin. The basin lies in the western margin of the Sino–Korean craton. It covers an area of approximately 2.5×10^5 km^2 and extends across five provinces (Shaanxi, Gansu, Ningxia, Inner Mongolia and Shanxi) (Fig. 1). The Ordos basin, which overlies a crystalline basement of Archean and Lower Proterozoic age, has been categorized as a flexural basin formed from EW directed thrusting resulting from the oblique collision of the Qiantang block with the Tarim–North China block in the Later Triassic (Watson et al., 1987). The Ordos basin started uplifting at the end of the Early Cretaceous during the Yanshanian Orogeny that is associated with the subduction of the Pacific plate (Yang et al., 2008).

Geographically, the Ordos plateau is separated from the North China plain by the NE trending Taihangshan mountain range, also known as the Trans North-China Orogen (TNCO). At the southern end of the plateau lies the Qinling orogenic belt which formed as a result of the collision between the North China and South China blocks during the Permian and Triassic (Fig. 1). To the southwest, the Ordos is bordered by the northeastern (NE) margin of the Tibetan plateau. The NE margin of the Tibetan plateau is featured by a series of parallel NW–SE trending mountain ranges, which were caused by thrusting and sinistral faulting (Tapponnier et al., 2001). The left-lateral strike slip Kunlun fault divides the margin into the Songpan–Ganzi block to the south and Tarim–Qilian block to the north (Fig. 1). The Songpan–Ganzi block was an accretionary prism formed during the northward subduction of the oceanic Qiantang lithosphere beneath the Tarim–North China block (Watson et al., 1987). Tapponnier et al. (2001) suggested that the rise of the Tibetan plateau occurred progressively from south to north, and that crustal thickening was accommodated by shortening along the compressional direction. On the other hand, Clark and Royden (2000) proposed that the topographic relief along the eastern and NE margins of the plateau is maintained by dynamic pressure from a lower crust flow. Injection of lower crustal material from the central plateau to the edges inflated the crust along the borders of the plateau. In other words, crustal thickening occurred mainly in the lower crustal level. Clark and Royden (2000) also found that steep and gentle slopes along the eastern and NE margins of the plateau could be explained by a rheological difference in the foreland, i.e., a difference in the strength of the tectonic blocks in the front of the margins. Based on their model, the Sichuan basin on the eastern side of the plateau has a strong keel, which effectively inhibited the eastward extrusion of the lower crustal flow from the plateau, resulting in a steep topographic slope along its eastern margin. On the other hand, the gentle slope along the NE corner of the Tibetan plateau was caused by a relatively weak crust beneath the Songpan–Ganzi terrane and the fold belts to the north. While crustal shortening

* Corresponding author. Geophysical Exploration Center, China Earthquake Administration, 75 Wenhua Road, Zhengzhou, Henan 450002, China. Tel.: +1 713 348 2515; fax: +1 713 348 5214.
E-mail address: sp11@rice.edu (S. Pan).

0012-821X/$ – see front matter © 2011 Elsevier B.V. All rights reserved.
doi:10.1016/j.epsl.2011.01.007

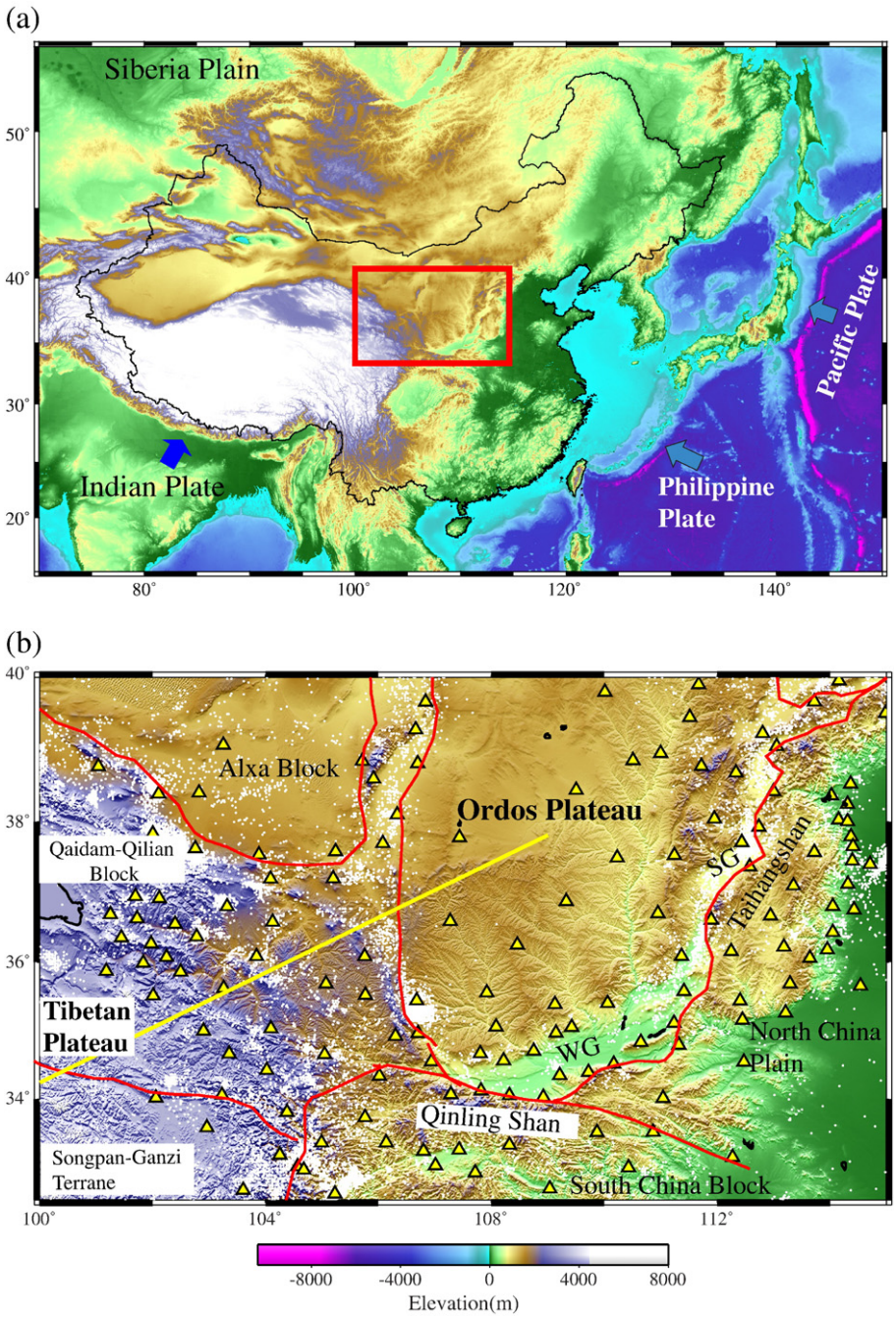

Fig. 1. (a) Map showing the major tectonic setting of Ordos plateau and the surrounding area. Arrows indicate the subduction of the Pacific and Philippine plates as well as the collision of the Indian plate on the east and southwest sides of China, respectively. The red rectangular region shows the location of the study area. (b) Topographic map showing the 154 broadband seismic stations (yellow triangles) from 10 regional seismic networks of the China Earthquake Administration. Microseismicity between 2001 and 2009 is shown in white dots. Red lines indicate boundaries between different tectonic blocks. WG and SG represent the Weihe graben and Shanxi graben, respectively. The yellow straight line shows the location of the refraction profile studied by Liu et al. (2006).

preserves the original composition of a crustal column, the lower crustal flow model predicts an overall mafic crust, as the thickened crust is comprised mainly of mafic lower crustal rocks, which was injected from the central plateau (Clark and Royden, 2000). In general mafic rocks have higher *Vp*/*Vs* ratios than felsic rocks (Christensen, 1996; Zandt and Ammon, 1995). Thus seismic measurements of *Vp*/*Vs* ratio across the area could be used to diagnose whether the crustal shortening model or the lower crustal flow model is a more appropriate explanation for the crustal thickening observed along the NE corner of the Tibetan plateau.

The Ordos basin is also a distinct block on the seismic map of China. While the plateau has virtually no seismic events, the rifts and fold belts surrounding the basin have very high seismic activities. Two historical magnitude 8 earthquakes occurred at the southeastern and eastern edges of the plateau. More recently, three magnitude 6 earthquakes, occurring at the northeastern edge of the basin were recorded in the 1990s. The large contrast in seismicity between the Ordos basin and the surrounding area makes it an ideal place to study the role of crust and lithosphere in controlling the overall strength of a plate.

The teleseismic P coda is comprised primarily of S waves converted from P waves at various depths below a station. The coda thus contains considerable information about the structure directly beneath the station. The receiver function technique is designed to isolate these P to S conversions (Langston, 1979; Owens et al., 1984) by deconvolution of a vertical (or longitudinal) component from a radial (or in-plane transverse) component in either the time or the frequency domain. Besides the P to S conversion, a receiver function also contains other coherent signals, such as the Moho reverberation phases, which are the multiple reflections from the free surface and the Moho. Recent receiver function studies have shown that one can estimate the average crustal *Vp*/*Vs* ratio and a better determined Moho depth with the arrival times of the conversion and the reverberation phases (Niu and James, 2002; Zandt and Ammon, 1995; Zhu and Kanamori, 2000). The crustal *Vp*/*Vs* ratio provides additional information that can help constrain the bulk composition of the continental crust.

With the rapid expansion of broadband seismic instrumentation in China in recent years, receiver function analysis has been widely used in estimating crustal thickness and *Vp*/*Vs* ratio in various parts of China. These studies, however, were conducted either at the local scale with temporarily deployed stations, or at the nationwide scale with the sparse national seismic network (Chen et al., 2010; Ma and Zhou, 2007). In this study, we took advantage of the recently released broadband data recorded by regional seismic networks operated by the China Earthquake Administration (CEA) (Fig. 1). We analyzed a large amount of receiver function data recorded by 11 regional networks to investigate lateral variations in crustal structure and composition and to understand the mechanism that controls the ongoing deformation and seismic activity in this region.

Fig. 2. Locations of the 105 teleseismic events (red solid circles) used in this study. Most of the earthquakes are located in the west, south Pacific and the Indonesia subduction zones. Note although some events fall into the 30° circle from the array center, all the seismograms we used has an epicentral distance between 30° and 90°.

2. Data and analysis

2.1. CEA regional network data

Completed in early 2007, the new CEA seismic network consists of a backbone national seismograph network, 31 provincial networks, and several small aperture arrays with more than 1000 stations including 850 ± broadband stations (Zheng et al., 2009). To study lateral variations in crustal structure and composition of the Ordos plateau and its surrounding areas, we selected 154 stations from 10 provincial networks located within the region of 100°–115°E and 32.5° to 40°N. We visually examined a total of 124 earthquakes with magnitude greater than 5.0 and located within the epicentral distance of 30°–90°, recorded between July of 2007 and early August of 2008. We chose 105 earthquakes with good signal-to-noise ratio (SNR). These earthquakes provide reasonably good distance and azimuthal coverage (Fig. 2), although a large portion of the events are clustered in the western Pacific and the Java trench with a back azimuth between 30° and 210°.

2.2. Receiver function analysis

We first rotated the two horizontal components of the seismograms to the radial and transverse components. Niu and Li (in press) found a significant portion of the CEA stations had problems with sensor orientation. We used their estimates of component azimuths, determined from the P-wave particle motion. The direct P wave is normally the dominant energy in the radial component and in the subsequent receiver function formed from it. The direct P wave could interfere with P to S conversions generated at shallow depths, such as at the base of a sediment layer. To minimize the P wave energy in the receiver function, we projected the two components to the principal directions (longitudinal and in-plane transverse), computed from the covariance matrix. The receiver functions were then computed from the data projected into this coordinate system (hereafter referred as to P- and SV-component) (Niu and Kawakatsu, 1998; Niu et al., 2007; Reading et al., 2003; Vinnik, 1977).

We employed the "water-level" deconvolution technique (Clayton and Wiggins, 1976) to generate receiver functions:

$$RF(\omega) = \frac{V(\omega)\cdot P^{*}(\omega)}{max\{|P(\omega)|^2,\ k\cdot|P_{max}(\omega)|^2\}} e^{-\left(\frac{\omega}{2a}\right)^2} \quad (1)$$

Here k and a are two constants that define "water level" and the corner frequency of the Gaussian low pass filter. k was set to be 0.01 and a was set to be 1.5, which is equivalent to a corner frequency of ~0.5 Hz. $P(w)$ and $V(w)$ are the spectra of the P and SV components. We used a 40 s time window (5 s and 35 s before and after the P wave) for M<7.0 earthquakes and a 100 s time window (5 s and 95 s before and after the P wave) for earthquakes with a magnitude greater than 7. We first visually inspected all the receiver functions and removed those with low SNR. At each station, we further calculated the covariance matrix of all the receiver functions and eliminated the ones that showed a low cross correlation coefficient (≤0.7) with other traces (Chen et al., 2010). We found most stations had more than 30 individual receiver functions. Fig. 3a shows an example of receiver functions recorded at SN.YAAN, a station located in the middle of the Ordos plateau. We also show the stacked receiver function in Fig. 3b. The primary P to S conversion and the two reverberation phases are clearly shown in the stacked receiver function (Fig. 3b). In this particular example, we can see the P to S conversion at the base of a thick sedimentary layer as well as the multiples. In general, we didn't find coherent and significant azimuthal variations in arrival time and amplitude of the primary P to S conversion phase from our data.

2.3. Depth stacking and H–κ analysis

Following Niu et al. (2007), we took two steps to measure crustal thickness and *Vp*/*Vs* ratio beneath each station. We first used a depth

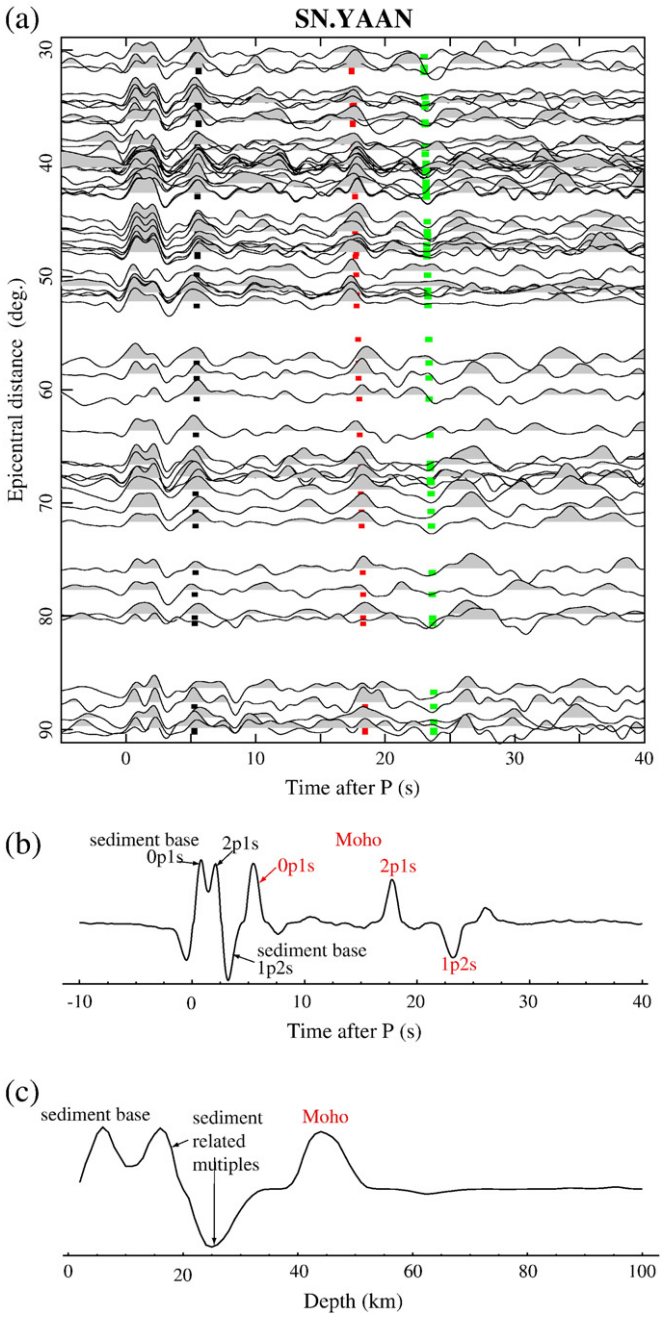

Fig. 3. (a) An example of the individual receiver functions recorded at station SN.YAAN located in the middle of the Ordos plateau. Square dots indicate the arrival times of the primary P to S conversion phase, 0p1s (black), and the two Moho reverberation phases, 2p1s (red) and 1p2s (green). Note 0p1s and 2p1s are clearly shown in most of the individual receiver functions. (b) The 2nd-root stacked receiver functions. P to S conversions at the base of the sediment layer and the crust are clearly shown. Multiple reflections between these boundaries and the surface are also clearly visible in the stacked receiver function. (c) The stacked receiver function after the time-to-depth conversion. The first two peaks and the first low in the stacked receiver function are associated with the sediment–basement boundary. The peak at around 42 km is the Moho.

stacking method to determine an initial depth of the Moho beneath a station. We then employed a refined H–k analysis to determine the final estimates of depth and V_P/V_S that best explain the observed P to S conversion and the reverberation phases. To obtain the initial depth, we first gathered receiver functions recorded at each station and made a time to depth conversion by assuming that P to S conversions are the primary sources of energy in the P-wave coda window. For a conversion depth, d, we first computed the relative arrival time of the converted phase, *Pds*, with respect to the direct arrival by ray tracing the two phases using a modified 1D iasp91 velocity model (Kennett and Engdahl, 1991), which has a low crust extending to depth d. We then summed the receiver function values averaged in a 0.1 s window centered on the arrival time of Pds using an Nth-root stacking technique (Kanasewich, 1973; Muirhead, 1968). Let $r_j(t)$ represents the jth receiver function recorded at a station, and τ_{dj} is the Pds arrival time for a Moho with a depth of d, an Nth-root stack, $R(d)$, is given by

$$R(d) = y(d)|y(d)|^{N-1} \tag{2}$$

where

$$y(d) = \frac{1}{K}\sum_{j=1}^{K} sign(r_j(\tau_{dj}))|r_j(\tau_{dj})|^{1/N} \tag{3}$$

Here K is the total event number recorded at the station. We chose $N=4$ to reduce the uncorrelated noise relative to the usual linear stack ($N=1$). We varied d from 0 to 100 km in an increment of 1 km. An example of the depth stacked receiver function is shown in Fig. 3c.

To better determine crustal thickness and *Vp/Vs*, we employed a tomographic velocity model derived from *P* travel times (Sun and Toksoz, 2006) to calculate the relative arrival times of the P to S conversion and the two reverberation phases with respect to the first arrival. The model has a 4-layer crust (sedimentary, upper, middle and lower crust) with a horizontal resolution of $1^\circ\times1^\circ$. For each station, we first found the nearest grid and then used its velocity profile as the 1D velocity model for the station. Assuming a Moho depth, H, and an average *Vp/Vs* ratio, κ, we then computed the relative arrival times of the primary P-to-S converted phase, 0p1s ($t1$), and the two crustal multiples, 2p1s ($t2$) and 1p2s ($t3$), with respect to the direct P wave using the following equations:

$$t_1 = H\left[\sqrt{\left(\frac{\kappa}{V_p}\right)^2 - p^2} - \sqrt{\left(\frac{1}{V_p}\right)^2 - p^2}\right] \tag{4a}$$

$$t_2 = H\left[\sqrt{\left(\frac{\kappa}{V_p}\right)^2 - p^2} + \sqrt{\left(\frac{1}{V_p}\right)^2 - p^2}\right] \tag{4b}$$

$$t_3 = 2H\sqrt{\left(\frac{\kappa}{V_p}\right)^2 - p^2} \tag{4c}$$

Here p is the P-wave ray parameter in s/km. We calculated p for each event-station pair based on the iasp91 velocity model. We also followed the phase notation of Niu and James (2002), *npms* means there are n P- and m S-wave legs within the crust. The receiver functions are then stacked:

$$s(H,\kappa) = \frac{c(\kappa)}{K}\sum_{i}^{K}\{w_1 r_i(t_1) + w_2 r_i(t_2) - w_3 r_i(t_3)\}. \tag{5}$$

Here K is the number of receiver functions at a given station and $r_i(t)$ represents the amplitude of the ith receiver function at the predicted arrival times. Considering the negative polarity of phase mode 1p2s, we assigned a negative sign to it in the summation. w_1, w_2 and w_3 are the weighting factors and were set to 0.5, 0.25 and 0.25, respectively. We also used all the combinations of the three phases in the H–κ analysis: 1) including all three phases, (2) using 0p1s and 1p2s phases, and (3) 0p1s and 2p1s phases only to ensure the consistency in measurement. In the case when only one of the multiples is used, the weight is set 0.7 for the primary and 0.3 for the multiple. Since the P to S conversion phase, 0p1s, usually has a higher SNR than the two multiples, we assigned a larger weight to it. Here we introduced a

coherence index of the three phases, $c(\kappa)$, to reduce the large tradeoff between H and κ in a regular H–κ stacking method (Zhu and Kanamori, 2000). A detailed comparison between the two methods can be found in Chen et al. (2010). We searched for H within ± 20 km of the initial depth determined from depth stacking. κ was varied in the range of 1.5 to 2 with an increment of 0.001. H and κ ratio were finally determined by picking the location where the summed amplitude, $s(H,\kappa)$, reaches its maximum. From the estimated Vp/Vs, we can calculate the Poisson's ratio:

$$\sigma = 0.5 - \frac{1}{2\{(V_P/V_S)^2 - 1\}}. \quad (6)$$

We show two examples of $s(H,\kappa)$ computed at one station located at the Ordos plateau (SN.YAAN, Fig. 4a) and another one on the Tibetan plateau (QH.LYX, Fig. 4b). For stations with undeveloped or inconsistent reverberation phases, which usually lead to unstable H–κ stacking or extreme Vp/Vs ratios, we used the Moho depth determined from depth stacking and kept the Vp/Vs ratio as undetermined.

3. Results and discussion

Among the 154 stations, we were able to obtain 143 measurements of Moho depth and 136 estimates of the Poisson's ratio (Fig. 5).

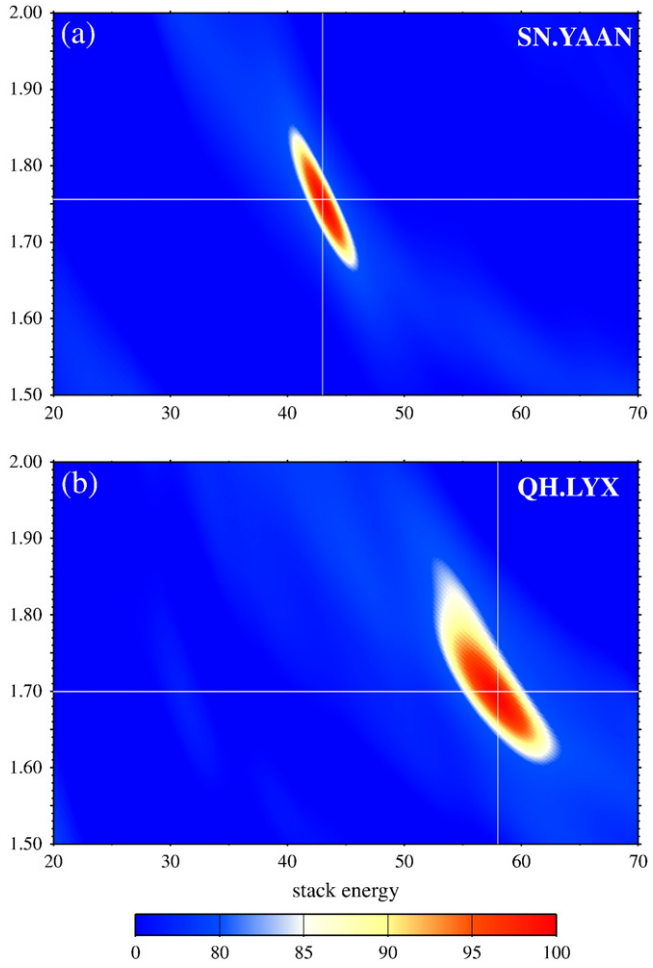

Fig. 4. Two examples of the "H–κ" analysis results obtained from stations SN.YAAN (a) and QH.LYX (b) located on the Ordos and Tibetan plateau, respectively. Color contours show the summed amplitude as a function of crustal thickness and Vp/Vs ratio. Location of the amplitude peak is indicated by the two white lines.

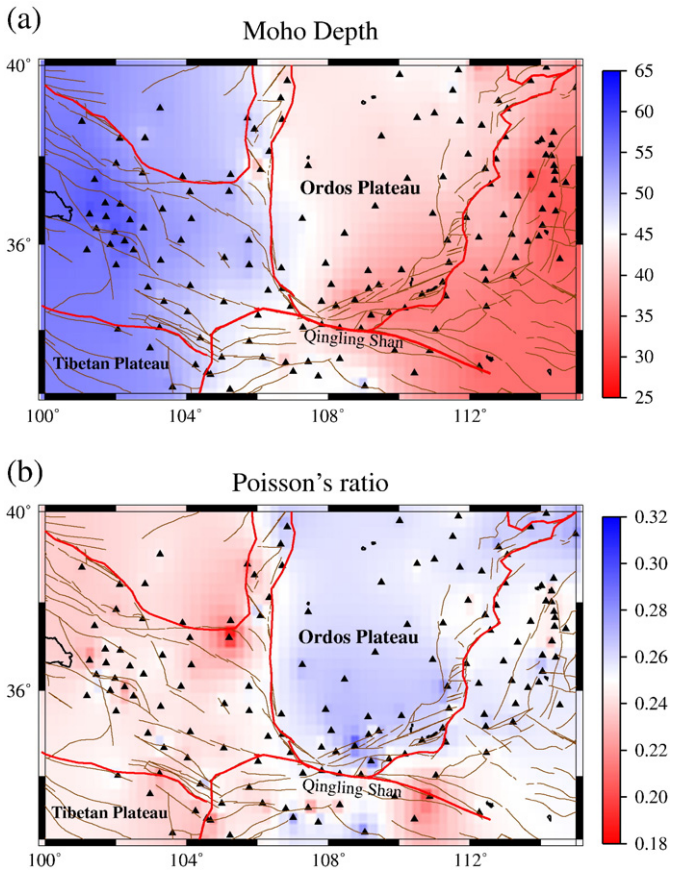

Fig. 5. Moho relief map inverted from observations at stations shown as black triangles. An inversion was performed to minimize the lateral variation of Moho depth (see Niu et al., 2007 for details). Note the gradual increase of Moho depth from east to west. Also note the thin crust beneath the Weihe graben at the southern edge of the Ordos plateau. (b) Map of lateral variations for the Poisson's ratio. The color contour is calculated from observations at stations shown by black triangles. The inversion method is the same as that used for Moho relief. Note a remarkable contrast between the Ordos and the Tibetan plateaus. Although the maps here were obtained from a regularized inversion, any decent interpolations are expected to yield more or less the same results.

The results are listed in Table S1. The table is organized by grouping stations in the following tectonic/physiographic regions: the Ordos plateau (OP), the Weihe graben (WG), the Qinling orogenic belt (QB), the Shanxi graben (SG), the Trans-North China orogen (TO), the North China plain (NP), the Alxa block (AX), and the northeastern margin of the Tibetan plateau (TP). In Table S1, we also showed 1σ errors, which were calculated based on a bootstrap method (Efron and Tibshirani, 1986). We note that these are formal errors, that do not include uncertainty in the velocity model, and actual errors are likely higher. There are three unknown parameters, Vp, H, and κ in Eqs. (4a)–(4c), and we made an assumption on Vp. It can be shown that κ is almost insensitive to Vp while H depends monotonically on the assumed Vp value. Chen et al. (2010) found that the model-induced uncertainty in Moho depth is expected to be $\lesssim$6–8%.

We used these measurements to generate 2D relief maps for Moho depth and Vp/Vs ratio respectively. We divided the study area from 32.5°N to 40°N (latitude) and 100°E to 115°E (longitude) into meshed grids of $0.25° \times 0.25°$. The total 1891 (31×61) unknown parameters of Moho depth were inverted from 143 observations. The kernel matrix has a dimension of 143×1891 with 143 non-zero elements ($=1$) that correspond to the 143 observations. A regularization that minimizes the first derivative of the model (the flattest Moho) is added to regularize the underdetermined inversion. Details of this algorithm were described in Niu et al. (2007). Similar to Moho depth, we also

inverted a 0.25°×0.25° *Vp*/*Vs* model from the 136 measurements (Fig. 5b). We must note here that the main purpose for generating the 2D maps is to demonstrate lateral variations in Moho depth and *Vp*/*Vs* ratio across the study area. The actual resolution is probably not as high as the 0.25°×0.25° grid spacing. Moreover, our data have no resolution in the corner regions; thus, they may not reflect the true values of the Moho depth and *Vp*/*Vs* ratio.

The resulting Moho relief map shows a highly variable crustal structure. The estimated Moho depths range from ~25 km beneath the north China plain to ~65 km beneath the northeastern margin of the Tibetan plateau. There is a good correlation between the estimated Moho depth and surface topography (between Figs. 1b and 5a; Fig. 6). In Fig. 6, we plotted 4 depth sections along the longitudinal and latitudinal directions, respectively. While the surface of the Ordos plateau is relatively flat with an elevation of ~1.2 km, the Moho depth changes significantly across the plateau. The Moho is located approximately 40 km below the mean sea level at the eastern edge of the plateau and deepens gradually towards the west, where it reaches ~50 km (Table 1, Fig. 6b and c). On the other hand there is no significant change in Moho depth in the NS direction. All of the receiver functions show significant P to S conversion and multiple reflections between the free surface and the sedimentary–bedrock boundary (Fig. 3b) at a few to ten kilometers deep (Fig. 3c). Watson et al. (1987) suggested that the Ordos plateau is an uplifted flexural basin controlled by eastward directed thrusting along its western margin. The observed thickening of the sedimentary cover and crustal thickness towards the west agrees with their interpretation of the origin of the Ordos basin.

Overall, the observed Moho depths appear to correlate roughly with the surface topography. The Moho beneath the Trans-North China Orogen east of the Ordos, however, shows no obvious deepening despite its high elevation (Figs. 5 and 6). The average Moho depth is ~40 km beneath the orogen. We found a rapid decrease in Moho depth as we move towards the east. The crust becomes as thin as ~25–30 km beneath the north China plain (Figs. 5 and 6). The thin crust suggests an extensional origin of the north China basin (Watson et al., 1987). The Moho also shows significant shallowing towards the south of the Ordos plateau. The shallowest Moho is located directly beneath the Weihe graben (~30 km), while its southern neighbor, the Qinling orogenic belt, has a thick crustal root extending to as deep as 45 km. In general, the crust beneath the NE margin of the Tibetan plateau is significantly thicker than the crust beneath the other areas; it varies from 55 to 65 km (Figs. 5 and 6). Our results are consistent with the results of two receiver function studies done with data from the national seismic network (Chen et al., 2010; Ma and Zhou, 2007). We also found a good agreement with results from active source data. Liu et al. (2006) studied a refraction profile that starts in the northern Songpan–Ganzi terrane and extends northeast to the Ordos plateau (yellow line in Fig. 1b). They found an increase in crustal thickness from 42 km beneath the Ordos plateau to 63 km beneath the Songpan–Ganzi terrane.

There is no simple correlation between the regional seismicity and crustal thickness observed here. Studies of rock mechanics indicated that most of the strength of continental lithosphere is contained in two separate strong zones, one in the middle crust and one in the upper mantle (e.g., Brace and Kohlstedt, 1980). It has been shown that a local increase in crustal thickness would reduce the size of the mantle strong zone without affecting the crustal strong zone, resulting in an overall weak lithosphere (Dunbar and Sawyer, 1988). The high seismicity observed at the NE margin of the Tibetan plateau might be attributed to a weak mantle lithosphere due to a thickened crust. On the other hand, we also found that the seismically active grabens, located at the margins of the Ordos plateau, have a relatively thin crust. This may be caused by a decrease in the size of the middle crustal strong zone due to extensional thinning of the crust in these regions (Dunbar and Sawyer, 1988). A better understanding of the seismic pattern in this region clearly requires more studies, and particularly studies of the entire lithosphere.

The Poisson's ratio map shown in Fig. 5b illustrates a remarkable contrast between the Ordos block and northeastern margin of Tibetan plateau: the Poisson's ratios measured from stations located at the Ordos block ($Vp/Vs = 1.761$, $\sigma = 0.261$) are systematically higher than

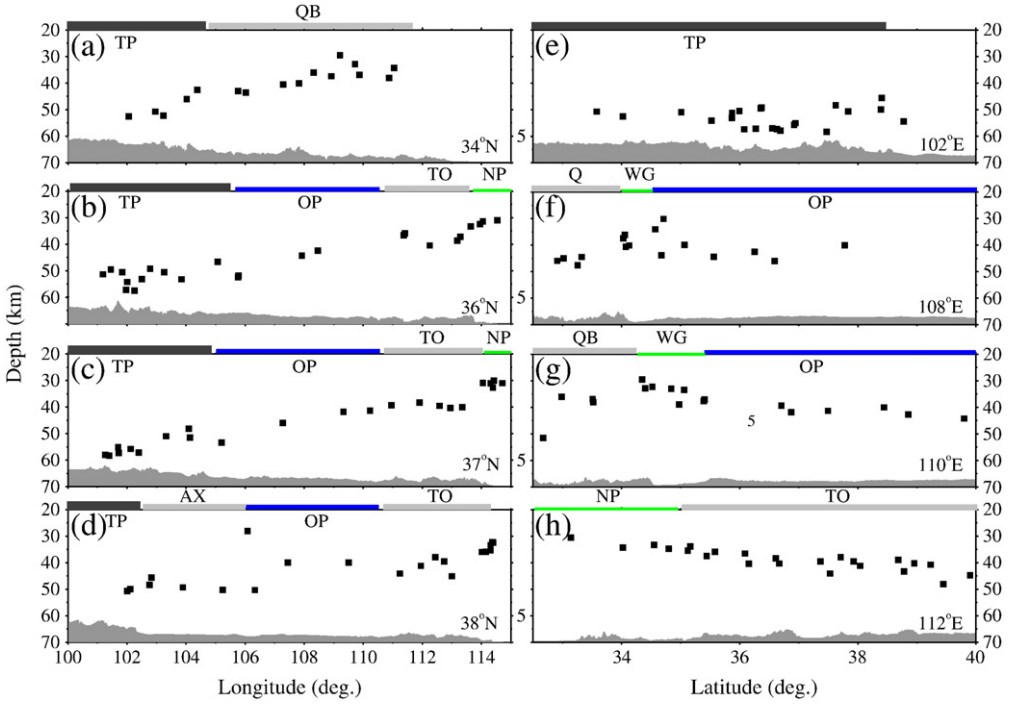

Fig. 6. Depth sections showing Moho depth varies along the longitudinal (a–d) and latitudinal direction (e–h), respectively. Thick solid lines at the top of each section indicate different tectonic blocks. AX: Alxa block; NP: North China plain; OP: Ordos plateau; QB: Qinling orogenic belt; TO: Trans-North China orogen; TP: Tibetan plateau; WG: Weihe graben. Section topography is shown at the bottom of each plot, with a scale shown in the middle of the two panels.

those from the NE margin of the Tibetan plateau ($Vp/Vs = 1.714$, $\sigma = 0.240$). Laboratory studies indicated that the compressional and shear wave velocity ratio, Vp/Vs, hence the Poisson's ratio, σ, is a good indicator of crustal composition (e.g., Christensen, 1996). Pressure and temperature appear to have little effect on it. The relative abundance of quartz ($Vp/Vs = 1.49$, $\sigma = 0.090$) and plagioclase ($Vp/Vs = 1.87$, $\sigma = 0.300$) has a dominant effect on the Poisson's ratio of common igneous rocks and their metamorphosed equivalents. An increase in plagioclase content or a decrease in quartz content can increase the Poisson's ratio of a rock. For example, the Poisson's ratio increases from 0.240 for granitic rock, to 0.269 for diorite, and to 0.300 for gabbro (Tarkov and Vavakin, 1982). The mafic/ultramafic igneous rocks generally have high Poisson's ratios because they usually contain gabbro and peridotite or dunite, which originate from magmatic differentiation. Moreover, partial melt has an important effect on the Poisson's ratio, which significantly increases with an increasing fluid fraction (Watanabe, 1993).

The lower Vp/Vs ratio observed beneath the NE margin of the Tibetan plateau is also consistent with the results of the refraction study by Liu et al. (2006). Liu et al. (2006) found the average P velocity and the Vp/Vs ratio of the crust in the Songpan–Ganzi region are both low, and suggested that the crust in the Songpan–Ganzi region is dominantly felsic in composition with an intermediate composition at the base. The felsic composition observed here disagrees with the average crustal composition predicted by the low crust channel flow model (Fig. 7a) proposed by Clark and Royden (2000). Based on this model, a crustal column in the NE margin of the Tibetan plateau is primarily composed of lower crustal material from central plateau. As a result, the average crustal composition would be mafic, leading to a high P-wave velocity and a high Vp/Vs ratio when the whole column is averaged. Hacker et al. (2000) studied the deep crustal xenoliths from the Tibetan plateau and found that the xenoliths were erupted from a depth of 30 to 50 km and were comprised of mafic rocks and siliciclastic metasedimentary rocks. The calculated Poisson's ratios of the xenoliths range from 0.258 to 0.272 with an average of 0.266. If lower crust materials with the same composition were injected into the margins of the Tibetan plateau, these margins would have showed a dominant high Vp/Vs ratio signature. However, because the observed the Vp/Vs ratios in the NE margin are systematically low, we speculate that shortening might be the dominant mechanism for producing the thick crust in this area (Fig. 7b). Since the Songpan–Ganzi terrane was the accretionary wedge before the Qiantang block collided with the Tarim–North China block, its composition is expected to be rather felsic, which may explain the observed low Vp/Vs ratios.

The flow model also seems to have problem with the explaining the thin crust beneath the Weihe graben. If the high elevation of Tibetan margin is maintained by dynamic pressure from a flow of low viscosity materials towards the Ordos basin and Sichuan basin to the south, then the Weihe graben should also gradually be filled by the Tibetan lower crust materials, resulting in a thick lower crust, which is not observed here. Rather, the Ordos basin appeared to be pushed away by the entire Tibetan lithosphere toward NNE. Consequently, a NW–SE extensional regime was created, leading to the formation of the Weihe graben.

Meanwhile, the observed Poisson's ratio $\sigma = 0.261$ at the Ordos block is very close to the global average of continental crust (0.265) (Christensen and Mooney, 1995). In a global study, Zandt and Ammon (1995) concluded that the crust of ancient shields is characterized by a relatively high Poisson's ratio (0.29), which is indicative of mafic material in the lowermost crust. The moderate value of the Poisson's ratio observed at the Ordos basin thus suggested that it could only accommodate relatively small amounts of granulite-facies mafic components. The lack of a high velocity mafic layer is indirectly supported by the large velocity contrast across the Moho, inferred from the large amplitude of conversion and reverberation phases. The

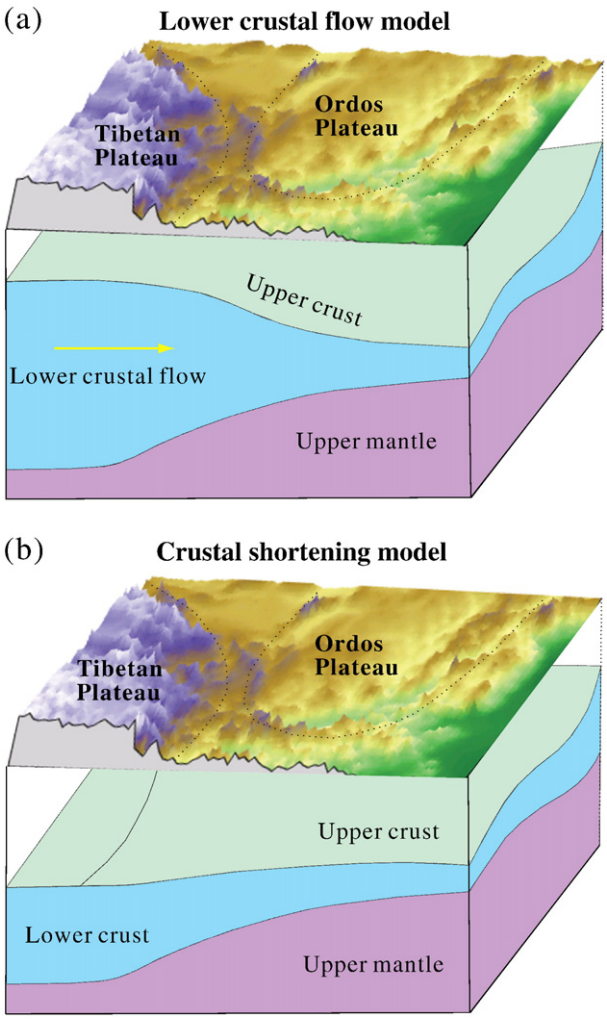

Fig. 7. Cartoon shows the two types of model responsible for crust thickening at the NE margin of the Tibetan Plateau: (a) lower crustal flow model; and (b) crustal shortening model. For each crustal column, the flow model (a) has a thicker lower crust, and thus is expected to have higher average crustal Vp/Vs ratio than the shortening model (b).

results here are consistent with observations in South Africa (Niu and James, 2002), South America (Niu et al., 2007) and west Australia (Durrheim and Mooney, 1994).

4. Conclusion

We investigated crustal structure beneath the Ordos plateau and its surrounding areas using waveform data recorded by 154 broadband seismic stations in the region. The receiver function data revealed the following features of the crust beneath the study area: (1) the crust beneath the uplifted Ordos basin is moderately thick (~42 km) and includes a thick sedimentary layer (~7 km). The estimated Poisson's ratio (0.261) suggests the crust is of intermediate composition. The Moho beneath the area is sharp and is accompanied by a large velocity/density contrast. All of these observations suggest the absence of a high velocity mafic layer in the lower crust beneath this stable part of the North China craton. (2) Crust beneath the northeastern margin of the Tibetan plateau varies from 55 to 65 km. The Vp/Vs ratio (1.714), and hence the Poisson's ratio (0.240), is remarkably low, indicating that the overall composition in this region is rather felsic. This seems to be inconsistent with a scenario of an inflated crust due to extrusion of mafic lower crust material from the Tibetan plateau to the margin. (3) The high seismicity observed in the NE margin of the Tibetan plateau and the grabens surrounding the

Ordos plateau is probably caused by a reduction in the size of the mantle and crustal strong zones, respectively.

Acknowledgements

We thank the Data Management Center of the China Earthquake Administration for providing waveform data for this study, H. Liu, S. Thurner, D.-R Wen for discussion, and two anonymous reviewers for their critical review and constructive comments, which significantly improved the quality of this paper. Some figures have been generated using the Generic Mapping Tools [Wessel and Smith, 1991]. S.P. is supported by NSFc grant 90814012 and F.N. is supported by the NSF grant EAR-063566. Contribution No. 201102, Geophysical Exploration Center, China Earthquake Administration.

Appendix A. Supplementary data

Supplementary data to this article can be found online at doi:10.1016/j.epsl.2011.01.007.

References

Brace, W.F., Kohlstedt, D.L., 1980. Limits on lithospheric stress imposed by laboratory experiments. J. Geophys. Res. 85, 6248–6252.
Chen, Y.L., Niu, F., Liu, R.F., Huang, Z.B., Tkalcic, H., 2010. Crustal structure beneath China from receiver function analysis. J. Geophys. Res. 115, B03307. doi:10.1029/2009JB006386.
Christensen, N.I., 1996. Poisson's ratio and crustal seismology. J. Geophys. Res. 101, 3139–3156.
Christensen, N.I., Mooney, W.D., 1995. Seismic velocity structure and composition of the continental crust: a global view. J. Geophys. Res. 100, 9761–9788.
Clark, M.K., Royden, L.H., 2000. Topographic ooze: building the eastern margin of Tibet by lower crustal flow. Geology 28, 703–706.
Clayton, R.W., Wiggins, R.A., 1976. Source shape estimation and deconvolution of teleseismic body waves. Geophys. J. R. Astron. Soc. 47, 151–177.
Dunbar, J.A., Sawyer, D., 1988. Continental rifting at pre-existing lithospheric weaknesses. Nature 333, 450–452.
Durrheim, R.J., Mooney, W.D., 1994. Evolution of the Precambrian lithosphere: seismological and geochemical constraints. J. Geophys. Res. 99, 15359–15374.
Efron, B., Tibshirani, R., 1986. Bootstrap methods for standard errors, confidence intervals, and other measures of statistical accuracy. Stat. Sci. 1, 54–75.
Hacker, B.R., Gnos, E., Ratschbacher, L., Grove, M., McWilliams, M., Sobolev, S., Wan, J., Wu, Z.H., 2000. Hot and dry deep crustal xenoliths from Tibet. Science 287, 2463–2466.
Kanasewich, E.R., 1973. Time Sequence Analysis in Geophysics. Univ. of Alberta Press, Edmonton, AB, p. 364.
Kennett, B.L.N., Engdahl, E.R., 1991. Travel times for global earthquake location and phase identification. Geophys. J. Int. 105, 429–465.
Langston, C.A., 1979. Structure under Mount Rainier, Washington, inferred from teleseismic body waves. J. Geophys. Res. 84, 4749–4762. doi:10.1029/JB084iB09p04749.
Liu, M.J., Mooney, W.D., Li, S.L., Okaya, N., Detweiler, S., 2006. Crustal structure of the northeastern margin of the Tibetan plateau from the Songpan–Ganzi terrane to the Ordos basin. Tectonophysics 420, 253–266.
Ma, Y., Zhou, H., 2007. Crustal thickness and Poisson's ratios in China by joint analysis of teleseismic receiver function and Rayleigh wave dispersion. Geophys. Res. Lett. 34, L12304. doi:10.1029/2007GL029848.
Muirhead, K.J., 1968. Eliminating false alarms when detecting seismic events automatically. Nature 217, 533–534.
Niu, F., James, D.E., 2002. Fine structure of the lowermost crust beneath the Kaapvaal craton and its implications for crustal formation and evolution. Earth Planet. Sci. Lett. 200, 121–130. doi:10.1016/S0012-821X(02)00584-8.
Niu, F., Kawakatsu, H., 1998. Determination of the absolute depths of the mantle transition zone discontinuities beneath China: effect of stagnant slabs on mantle transition zone discontinuities. Earth Planet. Space 50, 965–975.
Niu, F., Li, J., in press. Component azimuths of the CEArray stations estimated from P-wave particle motion, Earthquake Science.
Niu, F., Bravo, T., Pavlis, G., Vernon, F., Rendon, H., Bezada, M., Levander, A., 2007. Receiver function study of the crustal structure of the southeastern Caribbean plate boundary and Venezuela. J. Geophys. Res. 112, B11308. doi:10.1029/2006JB004802.
Owens, T.J., Zandt, G., Taylor, S.R., 1984. Seismic evidence for an ancient rift beneath the Cumberland Plateau, Tennessee: a detailed analysis of broadband teleseismic P waveforms. J. Geophys. Res. 89, 7783–7795. doi:10.1029/JB089iB09p07783.
Reading, A., Kennett, B.L.N., Sambridge, M., 2003. Improved inversion for seismic structure using transformed, S-wave vector receiver functions: removing the effect of the free surface. Geophys. Res. Lett. 30, 1981. doi:10.1029/2003GL018090.
Sun, Y., Toksoz, M.N., 2006. Crustal structure of China and surrounding regions from P wave traveltime tomography. J. Geophys. Res. 111, B03310. doi:10.1029/2005JB003962.
Tapponnier, P., Xu, Z.Q., Roger, F., Meyer, B., Arnaud, N., Wittlinger, G., Yang, J.S., 2001. Oblique stepwise rise and growth of the Tibet plateau. Science 294, 1671–1677.
Tarkov, A.P., Vavakin, V.V., 1982. Poisson's ratio behavior in crystalline rocks: application to the study of the Earth's interior. Phys. Earth Planet. Inter. 29, 24–29. doi:10.1016/0031-9201(82)90134-0.
Vinnik, L.P., 1977. Detection of waves converted from P to SV in the mantle. Phys. Earth Planet. Inter. 15, 39–45.
Watanabe, T., 1993. Effects of water and melt on seismic velocities and their application to characterization of seismic reflectors. Geophys. Res. Lett. 20 (2), 933–2936.
Watson, M.P., Hayward, A.B., Parkinson, D.N., Zhang, Z.M., 1987. Plate tectonic history, basin development and petroleum source rock deposition onshore China. Mar. Petrol. Geol. 4, 205–225.
Wessel, P., Smith, W.H.F., 1991. Free software helps map and display data. EOS Trans. Am. Geophys. Union 72, 441.
Yang, H., Fu, J.H., Wei, X.S., Liu, X.H., 2008. Sulige field in the Ordos basin: geological setting, field discovery and tight gas reservoirs. Mar. Petrol. Geol. 25, 387–400.
Zandt, G., Ammon, C.J., 1995. Continental crust composition constrained by measurement of crustal Poisson's ratio. Nature 374, 152–154.
Zheng, X.F., Ouyang, B., Zhang, D.N., Yao, Z.X., Liang, J.H., Zheng, J., 2009. Technical system construction of Data Backup Centre for China Seismograph Network and the data support to researches on the Wenchuan earthquake. Chin. J. Geophys. 52, 1412–1417. doi:10.3969/j.issn.0001-5733.2009.05.031. (in Chinese).
Zhu, L., Kanamori, H., 2000. Moho depth variation in southern California from teleseismic receiver functions. J. Geophys. Res. 105, 2969–2980.